



Published in final edited form as:

Nature. 2013 April 25; 496(7446): 533–536. doi:10.1038/nature12042.

Crystal structure of a eukaryotic phosphate transporter

Bjørn P. Pedersen¹, Hemant Kumar^{1,2}, Andrew B. Waight¹, Aaron J. Risenmay¹, Zgyg Roe-Zurz¹, Bryant H. Chau¹, Avner Schlessinger³, Massimiliano Bonomi³, William Harries¹, Andrej Sali³, Atul K. Johri², and Robert M. Stroud¹

¹Department of Biochemistry and Biophysics, University of California, San Francisco, CA 94158, United States of America.

²School of Life Sciences, Jawaharlal Nehru University, New Delhi-110067, India.

³Department of Bioengineering and Therapeutic Sciences, Department of Pharmaceutical Chemistry, California Institute for Quantitative Biosciences, University of California, San Francisco, CA 94158, United States of America.

Phosphate is crucial for structural and metabolic needs including nucleotide and lipid synthesis, signalling, and chemical energy storage. Essential for phosphate uptake in plants and fungi are proton-coupled transporters of the Major Facilitator Super-family (MFS), which also have a function in sensing external phosphate levels as transceptors^{1–5}. Here we report the 2.9 Å structure of a fungal high affinity phosphate importer, PiPT, in an inward-facing occluded state, with bound phosphate visible in the membrane buried binding site. The structure indicates both proton and phosphate exit pathways and suggests a modified asymmetrical 'Rocker-Switch' mechanism of phosphate transport. PiPT is related to several human transporter families, most notably the organic cation and anion transporters of the Solute Carrier Family (SLC22), which are implicated in cancer-drug resistance^{6,7}. We modelled representative cation and anion SLC22 transporters based on the PiPT structure to surmise the structural basis for substrate binding and charge selectivity in this important family. The PiPT structure demonstrates and expands on principles of substrate transport by the MFS transporters and illuminates principles of phosphate uptake in particular.

Users may view, print, copy, download and text and data- mine the content in such documents, for the purposes of academic research, subject always to the full Conditions of use: http://www.nature.com/authors/editorial_policies/license.html#terms

Correspondence and requests for materials should be addressed to R.M.S. (stroud@msg.ucsf.edu).

Author Contributions

B.P.P. did expression, purification and crystallization experiments, collected and processed the data, and determined, refined and analysed the structure. H.K. identified the target, did purification and crystallization experiments, collected data and identified the use of NG for crystallization. A.B.W. optimized the yeast expression system, and assisted in data collection and data analysis. A.R. helped with protein purification and crystallization. Z.R-Z. assisted in optimization of the yeast expression system, cloned, expressed, purified and characterized the target, and set up initial crystallization experiments. B.C. did cloning, expression tests and cell growth. A.Sc. performed bioinformatics analysis and built human homology models. M.B. did molecular dynamics and analysed the results. W.H. trained H.K. and assisted H.K. in data collection. A.S. supervised homology modelling, bioinformatics analysis and Molecular Dynamics. A.K.J. identified the target and initiated the project. R.M.S. supervised the project and analysed the structure. B.P.P. and R.M.S. wrote the paper with input from H.K., A.B.W., A.Sc., A.S. and A.K.J.

Author Information

Coordinates and structure factors have been deposited in the Protein Data Bank with the accession number 4J05. Reprints and permissions information is available at www.nature.com/reprints.

The Major Facilitator Super-family is the largest super-family of secondary active transporters and its diverse members generally function as symporters or antiporters driven by proton or sodium gradients¹. Structures of eight bacterial MFS transporters have been determined by 2D and 3D crystallography^{8–15}. Based on the first of these a 'Rocker-Switch' mechanism was proposed^{9,10}, suggesting that the symmetry related N- and C-domains rock back and forth as 'banana-shaped' rigid bodies with the central substrate binding site as the pivot point. However, structures of other MFS transporters in the occluded state adopt a compact arrangement of helices around the substrate binding site^{8,11,13} and a similarly occluded and compact structure for the Lactose Permease (LacY) has been suggested by molecular dynamics simulations¹⁶, double electron-electron resonance measurements¹⁷ and homology modeling¹⁸. This indicates that rigid body movements alone are not sufficient to explain translocation in the MFS super-family.

Piriformospora indica is an endophytic fungus that colonizes roots of many plant species and promotes growth¹⁹. We have recently shown the *P. indica* Phosphate Transporter (PiPT) to be a high affinity phosphate transporter involved in improving phosphate nutrition-levels in the host-plant²⁰. PiPT belongs to the Phosphate:H⁺ Symporter (PHS) family within the Major Facilitator Super-family¹. It is highly homologous to the *Saccharomyces cerevisiae* high affinity phosphate transporter, Pho84, and to plant phosphate transporters (Supplementary Fig. 1, Supplementary Table 1). It also shares homology with the human Solute Carrier alpha-group (SLC- α), especially the SLC22 family of human organic anion and cation transports, the SLC2 family of glucose facilitative transporters (GLUTs), and the related Synaptic Vesicle 2 Protein family (Supplementary Table 1)^{7,21,22}.

The structure of PiPT in complex with its substrate, inorganic phosphate, was determined to 2.9 Å resolution by experimental phasing (Fig. 1) and refined to a free crystallographic R-factor of 25.9% (Supplementary Figs. 2, 3 and 4, Supplementary Table 2). PiPT confirms that the MFS-fold found in bacteria is conserved in eukaryotes. PiPT has 12 transmembrane helices (M1-M12) divided into two homologous domains (N- and C-domain) related by a quasi-twofold symmetry perpendicular to the membrane plane. The structure includes residues 30 to 518 except for 67 residues in the flexible linker between N- and C-domain, predicted from sequence to be disordered. This disordered linker region in PiPT contains no discernible structure in the solved state of the protein, as seen in several other MFS structures^{10,13,14}. The linker has no sequence similarity to the four-helix bundle domain observed in the bacterial GLUT homologue Xyle¹⁵.

The overall conformation of PiPT is similar to structures of MFS transporters solved in the occluded state^{8,11,13} with the two domains forming a clam-shell like arrangement around a central membrane-buried binding site where the phosphate is bound. To the extracellular side of the binding site a cluster of 3 phenyl residues (F50, F327, F369) (Fig. 1a) block the entry pathway, and the distance from the phosphate site to the extracellular solvent is ~20 Å. The intracellular side of the binding site is also occluded but less so. The helix M4 blocks the cytosolic exit of the phosphate and about ~10 Å separate the phosphate from the solvent (Supplementary Fig. 5). We conclude that the structure captures the protein in an 'inward facing occluded state'²³.

Inorganic phosphate is located between the two domains buried in the middle of the membrane at a location similar to the substrate binding sites in other Major Facilitators^{9,13,15} (Fig. 1a). The phosphate is coordinated by Tyr150(M4), Gln177(M5), Trp320(M7), Asp324(M7), Tyr328(M7) and Asn431(M10) as well as by electrostatic interaction from the edge of Phe174(M5) (Fig. 1b). All these residues are fully conserved in the family of Phosphate:H⁺ symporters. Asp324(M7) coordinates the phosphate with both carboxyl oxygens (Fig. 1b). In Pho84, the corresponding residue (358) is essential for translocation, but initial phosphate-binding is unchanged by its replacement with an asparagine, mimicking a protonated aspartate²⁴. This suggests that the aspartate is protonated before engaging the phosphate. The conserved Lys459(M11) has been proposed to be involved in increasing the affinity for phosphate, with point-mutations causing a 2- to 3-fold decrease in affinity²⁴. In the PiPT structure, Lys459 is located next to the binding site with the lysine side-chain amine ~5 Å from the phosphate, too far away to interact with it (Supplementary Fig. 6). In this configuration, Lys459 could either play a role in initial outward facing phosphate binding, or possibly in charge compensation of Asp324 in the empty form of PiPT.

A tunnel is visible going from the binding site Tyr150 to the cytosol through the N-domain (Fig. 2, Supplementary Fig. 5). This cytosolic tunnel is substantially smaller (smallest diameter 1.2 Å) than phosphate, going from the binding site, between M4 and M1 towards the bottom of M3 and M6 leading to the cytosolic side. In the structure the cytosolic half of M4 is more flexible than the rest of the protein, as reflected in atomic displacement parameters that are almost twice as high as the surrounding residues (185 Å² vs. 107 Å²) (Fig. 2a, Supplementary Fig. 4e). Related to this flexibility, a conspicuous glycine-motif with four glycines is located at the middle of the M4 helix, introducing mobility by creating a hinge-region (Supplementary Fig. 7a).

Proton transfer through the membrane is expected to involve negatively charged residues^{12,14,23,25}. There are four negatively charged and conserved residues (Asp45(M1), Asp48(M1), Glu108(M3), Asp149(M4)) in the membrane embedded part of PiPT besides the key-residue Asp324 (Fig. 2a). Asp48 interacts with a buried Arg139 (Supplementary Fig. 6) and all the remaining residues are exposed to the cytosolic tunnel (Fig. 2b). In Pho84, the equivalent of Asp149 (178) has been proposed to be involved in transport at a later stage in the transport cycle than Lys459 (492) or Asp324 (358)²⁴. The location of these membrane buried carboxylates implicates the cytosolic tunnel in proton transfer to the cytosol.

The structure suggests a tentative model of phosphate-import by Phosphate:H⁺ symporters (Fig. 3). In the outward open state, Asp324 and other C-domain residues of the central binding site bind phosphate. Protonation of Asp324 lowers the energy barrier for phosphate binding and this ensures coupling between driving force and substrate translocation^{23,26}. Also, the aspartate helps to select protonated phosphate (phosphate monobasic) versus fully ionized divalent oxyanions like sulphates^{27–29}. Asp324 thus might have a dual role being the proton gatekeeper and ensuring substrate-specificity. As phosphate binds, N-domain residues move in and ensure an optimal fit, thereby repositioning the N-domain to close the entry pathway, forming the outward occluded state. Tyr150 located on the cytosolic side of the M4 glycine-motif interacts with the phosphate in the structure, shifting the flexible

region of the M4 helix to form the cytosolic tunnel. Via the tunnel, Asp45, Asp149 and Glu108 create a proton relay from the phosphate binding site to the cytosol that would allow protons to escape, but not permit the passage of phosphate. As positive charge is removed from the binding site along this relay, the binding of phosphate becomes unfavourable and the phosphate exit pathway between the two domains is forced open. In the structure M2 is slightly split apart from M11 at the cytosolic side, and from this conformation, release of the phosphate will require only small rearrangements of M4 and M5 to allow opening of the phosphate exit-pathway lined by the N-domain on one side and the C-domain on the other side (Supplementary Fig. 5). This opening movement seems stalled by 3 salt-bridges formed between the M4-M5 connecting loop and M8 in the structure (Asp159:Arg447, Arg165:Asp381, Arg166:Glu440). The sequential release of protons and then phosphate, with phosphate released between the two domains without major rearrangements is supported by Molecular Dynamics (Supplementary Fig. 8).

The glycine-motif in M4 could help create the suggested proton relay from the binding site to the cytosol and possibly help reposition the N-domain afterwards to allow phosphate to exit. The motif is fully conserved in the PHS family of proton/phosphate transporters (Supplementary Fig. 7a). The multidrug transporter, EmrD¹¹, and the oxalate/formate antiporter, OxIT⁸, both have glycine-rich motifs in M4 resembling those in PiPT (Supplementary Fig. 7b). Similar conserved motifs are found in sugar MFS transporters such as that found in M4 of the human SLC2 family of glucose facilitative transporters (GLUTs) (Supplementary Fig. 7c). In support of the proposed role of this motif in the inward facing conformation, the M4 helix does not appear as mobile in the outward facing occluded state of the bacterial GLUT homologue Xyle¹⁵. Further experiments will verify whether the M4-mobility observed here exists in other MFS families.

The PiPT structure is asymmetric in nature, with distinct functionality of the two domains. A similar division is also proposed for LacY, and the Peptide Transporter, PepT(so), where proton translocation is mediated mainly by the C-domain and substrate recognition mainly by the N-domain^{9,13,25}. Conversely, substrate recognition in PiPT is attained almost exclusively by the C-domain, while the mechanistic elements that allow translocation of protons and substrate are found in the more flexible N-domain.

Our proposed phosphate transporter model is compatible with the MFS Rocker-Switch mechanism, but with some notable modifications. It is consistent with an overall symmetry-related movement of the two domains during translocation, but suggests non-symmetrical intra-domain movements in the N-domain to assist proton translocation involving more complex dynamics.

To explore the impact of this structure on human homologues, we constructed homology models of two representative SLC22 members with different charge specificities: The organic cation transporter OCT1 and the organic anion transporter OAT3 (Supplementary Figs. 9 and 10, Supplementary Table 1). Neither model contains a negatively charged residue at the position corresponding to the proton gate-keeper Asp324, in agreement with the observation that SLC22 transporters are not driven by a proton gradient, but more likely by a sodium gradient⁷. The homology models did not allow us to confidently predict the

position of a possible sodium binding-site in OCT1 and OAT3, but the PiPT binding site residues on M7, Tyr328 and Trp320, are highly conserved in the SLC22 family, suggesting that members of this family share a similar substrate binding mechanism utilizing this helix. The charge of Lys459 is conserved at the corresponding position in the organic anion transporters (e.g., Arg454 in OAT3), but is reversed in the organic cation transporters (e.g., Asp474 in OCT1), consistent with a pivotal role in substrate charge specificity³⁰. Finally, the predicted binding pockets in OCT1 and OAT3 are larger than those in PiPT, in agreement with their broader substrate specificities (Supplementary Fig. 9).

In summary, this first structure of a eukaryotic MFS member explains structural/functional relationships of phosphate/proton symport by providing structural evidence for phosphate affinity and specificity and connecting the proton-motive force to phosphate translocation. PiPT provides a strong template for modelling key transporters whose malfunctions in humans are associated with diseases such as cancer and diabetes (e.g., MCT-1 and GLUT4), as well as those that mediate drug absorption, distribution and elimination (e.g., OCT1). These findings provide new insights into charged ligand recognition, binding and release in the context of active membrane transport, a process essential to all living cells.

Methods Summary

The *Piriformospora indica* high affinity phosphate transporter PiPT (accession number A8N031) was expressed in *Saccharomyces cerevisiae* and purified using a polyhistidine affinity-tag. Solubilization and purification used dodecyl-beta-D-maltoside followed by nonyl-beta-D-glucoside. Crystals were grown by vapour diffusion. Crystallographic data were collected at the Advanced Light Source beamline 8.3.1 and later at Advanced Photon Source beamline 23-ID-B and 23-ID-D. All crystals showed clear signs of hemihedral twinning with a variable twin-fraction from 0.14 to 0.47. Experimental phases were determined using derivative crystals containing K_2PtCl_6 or $(Ta_6Br_{12})Br_2$. Heavy-atom derived phases were refined and extended to the maximum resolution of the native data by density modification, exploiting histogram mapping, solvent flattening with a solvent content of 73%, two-fold non-crystallographic symmetry and four-fold inter-crystal averaging. Final refinement using data to 2.9 Å resolution produced a structural model with a crystallographic R-factor of 22.2% and a free R-factor of 25.9% (Supplementary Table 2).

Methods

Sample preparation

A 2-micron *Saccharomyces cerevisiae* expression construct based on p423_GAL1³¹ contained nucleotides coding for the *Piriformospora indica* high affinity phosphate transporter PiPT (accession number A8N031) as well as N-terminal and C-terminal purification-tags as described³². Transformed *S. cerevisiae* (strain DSY-5) were grown in a 15 l culture vessel (Biostat C15L Sartorius AG) to high density and induction was done in fed-batch using 40% galactose, and harvested after a 16 hour induction. Harvested yeast were washed in cold water, spun down and resuspended in Lysis-buffer (100 mM Tris pH 7.5, 600 mM NaCl, 1 mM EDTA, 1 mM tris(2-carboxyethyl)phosphine (TCEP), 1.2 mM phenylmethylsulfonyl fluoride) before lysis by bead beating using 0.5 mm glass-beads. The

homogenate was centrifuged for 25 minutes at 21,600 g, followed by sedimentation of membranes by ultracentrifugation at 185,000 g for 150 minutes. Membrane pellets were resuspended in Membrane-buffer (50 mM Tris pH 7.5, 500 mM NaCl, 20% Glycerol) before being frozen in liquid nitrogen in 3 g aliquots. A normal yield was 20–25 g membrane-pellet from 100 g cells. 3 g membrane were solubilized for 30 minutes in Membrane-buffer using 300 mg n-dodecyl-beta-D-maltoside (DDM) (1:10 (w/w) ratio) in a total volume of 50 ml, after which unsolubilized material was removed by filtration using a 1.2 μm filter. 20 mM imidazole pH 7.5 were added and the solubilized membranes loaded on a pre-equilibrated 1 ml Ni-NTA column (GE Healthcare) at 1 ml/min. After loading, the column was washed with 20 column-volumes of W100-buffer (Membrane buffer supplemented with 100 mM Imidazole pH 7.5, 1 mM TCEP, 10 mM K_2HPO_4 and 0.05% DDM), and eluted in 5 ml G-buffer (50 mM MES pH 6.5, 200 mM NaCl, 10 mM K_2HPO_4 , 0.5 mM TCEP, 0.2% n-nonyl-beta-D-glucoside (NG)) supplemented with 500 mM Imidazole pH 7.5. To remove purification tags, Bovine Thrombin and HRV 3C Protease were added and the sample dialyzed for 16 hours against 100 ml G-buffer. A normal yield was 10 mg pure PiPT from 3 g of membrane. After dialysis the sample was concentrated using a spin-column (50 kDA cut-off, Amicon) to 500 μl and injected on a size-exclusion column (Superdex 200, GE Healthcare) pre-equilibrated in G-buffer. Peak fractions were concentrated to 10–15 mg/ml before a new dialysis for 16 hours against 100 ml G-buffer. An ultracentrifugation spin (108,000 g, 20 minutes) was applied before crystallization setup.

Crystal Growth

Crystals were grown at 20°C by vapour diffusion in 2+2 μl hanging drops with a reservoir containing 26–29% (w/v) Pentaerythritol propoxylate (5/4 PO/OH), 6–11% Polyethylene glycol 400, 200 mM KCl and 100 mM Sodium Citrate pH 5.5. Hexagonal crystals, with a final size of around 200x200x50 μm , were obtained after typically one week of crystal-growth but would be extremely sporadic in appearing (Supplementary Fig. 2a). Crystals grew in DDM, DM and NG, but morphology and space group changed in NG, and diffraction improved from 4–6 \AA to 2.9 \AA in the best case. Data were collected at the Advanced Light Source beamline 8.3.1 and later at the Advanced Photon Source beamline 23-ID-B and 23-ID-D. Initial crystals displayed ~ 10 \AA resolution, with severely split spots. Several lines of crystal improvement augmented diffraction properties. Optimized crystals normally diffracted isotropically to 3.2 \AA , with a single crystal screened extending to 2.9 \AA (Supplementary Fig. 2a). Heavy-atom derivatives were obtained by adding K_2PtCl_6 or $(\text{Ta}_6\text{Br}_{12})\text{Br}_2$ to the crystals a day prior to flash-cooling, either as salt or as a concentrated, aqueous solution.

Data processing

Data sets were processed using XDS³³ in space group *R* 3. The data showed clear signs of hemihedral twinning with the twin law (k,h,-l) (Supplementary Table 2). The estimated twin fraction varied from 0.14 to 0.47. The data was detwinned using DETWIN from the CCP4 suite³⁴. Extensive molecular replacement was attempted essentially as described³⁵ but was unsuccessful in solving the phase problem. Initial heavy-atom positions of two platinum sites were found by SIRAS in SHELXC/D³⁶ using detwinned datasets where the estimated twin-fraction was matched between datasets and minimized as much as possible³⁷. A single

Ta₆Br₁₂-cluster site were identified using the initial platinum phases, and experimental MIRAS phases combining two platinum sites and one Ta₆Br₁₂-cluster site were calculated to 3.5 Å in SHARP³⁸ using detwinned datasets (Supplementary Fig. 2b). Gross map-features (e.g. number of discernible α -helices) were significantly improved when experimental phases and maps were calculated from detwinned data as opposed to twinned data. Heavy-atom-derived phases were refined, combined and extended at the maximum resolution of the native data by density modification in DMMULTI³⁹ exploiting histogram mapping, solvent flattening with a solvent content of 73%, two-fold non-crystallographic symmetry and four-fold inter-crystal averaging. It was helpful to start phase extension at low resolution (10 Å) and very gradually extend (2000 cycles) to the full resolution of the data^{35,40}. The resulting electron-density map was of good quality given the low phasing power, providing a continuous trace of the main-chain (Supplementary Table 2, Supplementary Fig. 4). Iterative model building in *O*⁴¹ and refinement in phenix.refine⁴² gradually improved the model and the fit to the experimental map. At later stages model-building was guided by 2mFo-dFc maps using model-phases. Final refinement in phenix.refine used 2-fold torsion-NCS with a refinement strategy of individual sites, individual ADP, occupancy (phosphate only) and TLS (4 groups), against a maximum likelihood (ML) target with reflections in the 69–2.9 Å range of the detwinned dataset (Supplementary Table 2). Refinement could also be done directly against the twinned data using a modified least-squares target ('twin_lsq_f'), but the resulting model was of poorer quality as reflected in worse R-factors and poorer electron-density in the maps for omitted regions. This might be caused by the usage of a least-squares target which disfavours the usage of weak reflections⁴³. The final resolution cut-off was based on the behaviour of the crystallographic R-factor (R_{work}) in 0.1 Å resolution shells to ensure full utilization of the data. We deemed that an R_{work} below 40% meant the data in the given resolution shell was effectively contributing beneficially to the model. The selected cut-off of 2.9 Å based on this approach correlated with an intra-dataset correlation coefficient $CC_{1/2}$ ⁴⁴ of 25%. The final model yielded a crystallographic R-factor of 22.2% and a free R-factor of 25.9%. MolProbity⁴⁵ evaluation of the Ramachandran plot gave 89.5% in favoured regions, and 2.6% outliers as expected for this resolution. The cytosolic tunnel was visualized using Mole⁴⁶. Electrostatic surfaces were calculated using APBS⁴⁷. All structural figures were prepared using PyMOL⁴⁸.

Homology Modelling

Alignments between sequences and PiPT were calculated using MUSCLE⁴⁹ and PROMALS3D⁵⁰, followed by manually refining gaps based on the transmembrane regions observed in the PiPT structure and predicted for other sequences using Phobius⁵¹. Homology models of OCT1 (SLC22A1) and OAT3 (SLC22A8) were constructed using MODELLER-9v11⁵² and assessed using Z-DOPE⁵³, a normalized atomic distance-dependent statistical potential based on known protein structures. Side-chains of selected residues in the initial OCT1 (Lys214 and Asp474) and OAT3 (Asn450 and Arg454) models were then refined using Scwrl4⁵⁴.

Molecular Dynamics

Simulations were performed with GROMACS⁵⁵, using the CHARMM27⁵⁶ all-atom force field and the TIP3P⁵⁷ water model. Topology and charges for the phosphate ion were

generated with ParamChem.org⁵⁸. PiPT was oriented in an implicit lipid bilayer using PPM⁵⁹, then immersed in a explicit 1,2-Dimyristoyl-*sn*-Glycero-3-Phosphocholine (DMPC) lipid bilayer and water using CHARMM-GUI⁶⁰. Periodic boundary conditions and a triclinic box with volume of 557.7 nm³ were used. PiPT was simulated a) at neutral pH and b) with two protons added to Asp45 and Asp324. Equilibration was performed by three 10ns long runs, gradually increasing the temperature from 100K to 300K, in the canonical (*NVT*) ensemble controlled by the Berendsen⁶¹ thermostat. The positions of non-hydrogen atoms of PiPT were restrained by a harmonic potential, with gradually decreasing intensity. A final equilibration step was carried out for 10ns without restraints, in the isothermal–isobaric (*NpT*) ensemble controlled by the semi-isotropic Berendsen⁶¹ barostat. Each production run was 100ns long, in the *NpT* ensemble controlled by the Bussi-Donadio-Parrinello⁶² thermostat and the semi-isotropic Parrinello-Rahman⁶³ barostat.

Supplementary Material

Refer to Web version on PubMed Central for supplementary material.

Acknowledgements

We thank Kathleen Giacomini for discussions about SLC transporters; Poul Nissen for helpful comments that improved the manuscript; James Holton, George Meigs, Craig Ogata and Nagarajan Venugopalan for assistance with synchrotron data collection at the Advanced Light Source and Advanced Photon Source; and Christopher Waddling, Pascal Wassam and Meseret Tessema for technical assistance. B.P.P. was supported by a Postdoctoral fellowship from the Carlsberg Foundation and later by a fellowship from the Danish Cancer Society; H.K. by a fellowship from Woods Whelan foundation, Council of Scientific and Industrial Research, Govt. of India and a travel grant from Jawaharlal Nehru University, New Delhi.; A.Sc by NIH postdoctoral fellowship F32 GM088991; A.S. by NIH grants U54 GM094625 and U01 GM61390; A.K.J. by a Research Assistant Professorship to do work at UCSF from the American Society for Microbiology; and R.M.S. by NIH grants U54 GM094625, GM24485 and GM073210.

References

1. Pao SS, Paulsen IT, Saier MH Jr. Major facilitator superfamily. *Microbiol. Mol. Biol. Rev.* 1998; 62:1–34. [PubMed: 9529885]
2. Persson BL, et al. Regulation of phosphate acquisition in *Saccharomyces cerevisiae*. *Curr. Genet.* 2003; 43:225–244. [PubMed: 12740714]
3. Nussaume L, et al. Phosphate Import in Plants: Focus on the PHT1 Transporters. *Front Plant Sci.* 2011; 2:83. [PubMed: 22645553]
4. Giots F, Donaton MCV, Thevelein JM. Inorganic phosphate is sensed by specific phosphate carriers and acts in concert with glucose as a nutrient signal for activation of the protein kinase A pathway in the yeast *Saccharomyces cerevisiae*. *Mol. Microbiol.* 2003; 47:1163–1181. [PubMed: 12581367]
5. Popova Y, Thayumanavan P, Lonati E, Agrochao M, Thevelein J. Transport and signaling through the phosphate-binding site of the yeast Pho84 phosphate transceptor. *Proc. Natl. Acad. Sci. U.S. A.* 2010; 107:2890–2895. [PubMed: 20133652]
6. Giacomini KM, et al. Membrane transporters in drug development. *Nat Rev Drug Discov.* 2010; 9:215–236. [PubMed: 20190787]
7. Hediger MA, et al. The ABCs of solute carriers: physiological, pathological and therapeutic implications of human membrane transport proteins. *Pflugers Arch.* 2004; 447:465–468. [PubMed: 14624363]
8. Hirai T, et al. Three-dimensional structure of a bacterial oxalate transporter. *Nat. Struct. Biol.* 2002; 9:597–600. [PubMed: 12118242]
9. Abramson J, et al. Structure and mechanism of the lactose permease of *Escherichia coli*. *Science.* 2003; 301:610–615. [PubMed: 12893935]

10. Huang Y, Lemieux MJ, Song J, Auer M, Wang DN. Structure and mechanism of the glycerol-3-phosphate transporter from *Escherichia coli*. *Science*. 2003; 301:616–620. [PubMed: 12893936]
11. Yin Y, He X, Szweczyk P, Nguyen T, Chang G. Structure of the multidrug transporter EmrD from *Escherichia coli*. *Science*. 2006; 312:741–744. [PubMed: 16675700]
12. Dang S, et al. Structure of a fucose transporter in an outward-open conformation. *Nature*. 2010; 467:734–738. [PubMed: 20877283]
13. Newstead S, et al. Crystal structure of a prokaryotic homologue of the mammalian oligopeptide-proton symporters, PepT1 and PepT2. *EMBO. J.* 2011; 30:417–426. [PubMed: 21131908]
14. Solcan N, et al. Alternating access mechanism in the POT family of oligopeptide transporters. *EMBO. J.* 2012; 31:3411–3421. [PubMed: 22659829]
15. Sun L, et al. Crystal structure of a bacterial homologue of glucose transporters GLUT1-4. *Nature*. 2012; 490:361–366. [PubMed: 23075985]
16. Holyoake J, Sansom MSP. Conformational change in an MFS protein: MD simulations of LacY. *Structure*. 2007; 15:873–884. [PubMed: 17637346]
17. Smirnova I, et al. Sugar binding induces an outward facing conformation of LacY. *Proc. Natl. Acad. Sci. U.S.A.* 2007; 104:16504–16509. [PubMed: 17925435]
18. Madej MG, Soro SN, Kaback HR. Apo-intermediate in the transport cycle of lactose permease (LacY). *Proc. Natl. Acad. Sci. U.S.A.* 2012 doi: 10.1073/pnas.1211183109.
19. Varma A, Bakshi M, Lou B, Hartmann A, Oelmueller R. *Piriformospora indica*: A Novel Plant Growth-Promoting Mycorrhizal Fungus. *Agricultural Research*. 2012; 1:117–131.
20. Yadav V, et al. A phosphate transporter from the root endophytic fungus *Piriformospora indica* plays a role in phosphate transport to the host plant. *J. Biol. Chem.* 2010; 285:26532–26544. [PubMed: 20479005]
21. Fredriksson R, Nordström KJV, Stephansson O, Häggglund MGA, Schiöth HB. The solute carrier (SLC) complement of the human genome: phylogenetic classification reveals four major families. *FEBS Lett.* 2008; 582:3811–3816. [PubMed: 18948099]
22. Schlessinger A, et al. Comparison of human solute carriers. *Protein Sci.* 2010; 19:412–428. [PubMed: 20052679]
23. Forrest LR, Krämer R, Ziegler C. The structural basis of secondary active transport mechanisms. *Biochim. Biophys. Acta.* 2011; 1807:167–188. [PubMed: 21029721]
24. Samyn DR, et al. Mutational analysis of putative phosphate- and proton-binding sites in the *Saccharomyces cerevisiae* Pho84 phosphate:H(+) transceptor and its effect on signalling to the PKA and PHO pathways. *Biochem. J.* 2012; 445:413–422. [PubMed: 22587366]
25. Kaback HR, Smirnova I, Kasho V, Nie Y, Zhou Y. The alternating access transport mechanism in LacY. *J. Membr. Biol.* 2011; 239:85–93. [PubMed: 21161516]
26. Krupka RM. Coupling mechanisms in active transport. *Biochim. Biophys. Acta.* 1993; 1183:105–113. [PubMed: 8399371]
27. Luecke H, Quioco FA. High specificity of a phosphate transport protein determined by hydrogen bonds. *Nature*. 1990; 347:402–406. [PubMed: 2215649]
28. Vyas NK, Vyas MN, Quioco FA. Crystal structure of *M tuberculosis* ABC phosphate transport receptor: specificity and charge compensation dominated by ion-dipole interactions. *Structure*. 2003; 11:765–774. [PubMed: 12842040]
29. Morales R, et al. Serendipitous discovery and X-ray structure of a human phosphate binding apolipoprotein. *Structure*. 2006; 14:601–609. [PubMed: 16531243]
30. Feng B, Dresser MJ, Shu Y, Johns SJ, Giacomini KM. Arginine 454 and lysine 370 are essential for the anion specificity of the organic anion transporter, rOAT3. *Biochemistry*. 2001; 40:5511–5520. [PubMed: 11331016]
31. Mumberg D, Müller R, Funk M. Regulatable promoters of *Saccharomyces cerevisiae*: comparison of transcriptional activity and their use for heterologous expression. *Nucleic Acids Res.* 1994; 22:5767–5768. [PubMed: 7838736]
32. Li M, et al. Selecting optimum eukaryotic integral membrane proteins for structure determination by rapid expression and solubilization screening. *J. Mol. Biol.* 2009; 385:820–830. [PubMed: 19061901]

33. Kabsch W. XDS. *Acta Crystallographica Section D Biological Crystallography*. 2010; 66:125–132.
34. Winn MD, et al. Overview of the CCP4 suite and current developments. *Acta Crystallographica Section D Biological Crystallography*. 2011; 67:235–242.
35. Pedersen BP, Morth JP, Nissen P. Structure determination using poorly diffracting membrane protein crystals - Lessons from the H⁺ and Na⁺,K⁺-ATPases. *Acta Crystallographica Section D Biological Crystallography*. 2010; 66:309–313.
36. Sheldrick GM. Experimental phasing with SHELXC/D/E: combining chain tracing with density modification. *Acta Crystallographica Section D Biological Crystallography*. 2010; 66:479–485.
37. Terwisscha van Scheltinga AC, Valegård K, Hajdu J, Andersson I. MIR phasing using merohedrally twinned crystals. *Acta Crystallographica Section D Biological Crystallography*. 2003; 59:2017–2022.
38. Bricogne G, Vonrhein C, Flensburg C, Schiltz M, Paciorek W. Generation, representation and flow of phase information in structure determination: recent developments in and around SHARP 2.0. *Acta Crystallographica Section D Biological Crystallography*. 2003; 59:2023–2030.
39. Cowtan K. 'dm': An automated procedure for phase improvement by density modification. *CCP4 Newsletter in Protein Crystallography*. 1994; 31:34–38.
40. Keller S, Pojer F, Heide L, Lawson DM. Molecular replacement in the 'twilight zone': structure determination of the non-haem iron oxygenase NovR from *Streptomyces spheroides* through repeated density modification of a poor molecular-replacement solution. *Acta Crystallographica Section D Biological Crystallography*. 2006; 62:1564–1570.
41. Jones TA, Zou JY, Cowan SW, Kjeldgaard M. Improved methods for building protein models in electron density maps and the location of errors in these models. *Acta Crystallographica Section A*. 1991; 47(Pt 2):110–119.
42. Adams PD, et al. PHENIX: a comprehensive Python-based system for macromolecular structure solution. *Acta Crystallographica Section D Biological Crystallography*. 2010; 66:213–221.
43. McCoy AJ. Liking likelihood. *Acta Crystallographica Section D Biological Crystallography*. 2004; 60:2169–2183.
44. Karplus PA, Diederichs K. Linking crystallographic model and data quality. *Science*. 2012; 336:1030–1033. [PubMed: 22628654]
45. Chen VB, et al. MolProbity: all-atom structure validation for macromolecular crystallography. *Acta Crystallographica Section D Biological Crystallography*. 2010; 66:12–21.
46. Petek M, Košinová P, Kosa J, Otyepka M. MOLE: A Voronoi Diagram-Based Explorer of Molecular Channels, Pores, and Tunnels. *Structure*. 2007; 15:1357–1363. [PubMed: 17997961]
47. Baker NA, Sept D, Joseph S, Holst MJ, McCammon JA. Electrostatics of nanosystems: Application to microtubules and the ribosome. *Proc. Natl. Acad. Sci. U.S.A.* 2001; 98:10037–10041. [PubMed: 11517324]
48. Schrödinger, L. The PyMOL Molecular Graphics System, Version 1.5.0.4.
49. Edgar RC. MUSCLE: multiple sequence alignment with high accuracy and high throughput. *Nucleic Acids Res.* 2004; 32:1792–1797. [PubMed: 15034147]
50. Pei J, Kim B-H, Grishin NV. PROMALS3D: a tool for multiple protein sequence and structure alignments. *Nucleic Acids Res.* 2008; 36:2295–2300. [PubMed: 18287115]
51. Käll L, Krogh A, Sonnhammer ELL. A combined transmembrane topology and signal peptide prediction method. *J. Mol. Biol.* 2004; 338:1027–1036. [PubMed: 15111065]
52. Sali A, Blundell TL. Comparative protein modelling by satisfaction of spatial restraints. *J. Mol. Biol.* 1993; 234:779–815. [PubMed: 8254673]
53. Shen M-Y, Sali A. Statistical potential for assessment and prediction of protein structures. *Protein Sci.* 2006; 15:2507–2524. [PubMed: 17075131]
54. Krivov GG, Shapovalov MV, Dunbrack RL Jr. Improved prediction of protein side-chain conformations with SCWRL4. *Proteins*. 2009; 77:778–795. [PubMed: 19603484]
55. Hess B, Kutzner C, van der Spoel D, Lindahl E. GROMACS 4: Algorithms for highly efficient, load-balanced, and scalable molecular simulation. *J Chem Theory Comput*. 2008; 4:435–44. [PubMed: 26620784]

56. Bjelkmar P, Larsson P, Cuendet MA, Hess B, Lindahl E. Implementation of the CHARMM Force Field in GROMACS: Analysis of Protein Stability Effects from Correction Maps, Virtual Interaction Sites, and Water Models. *J Chem Theory Comput.* 2010; 6:459–466. [PubMed: 26617301]
57. Jorgensen WL, Chandrasekhar J, Madura JD, Impey RW, Klein ML. Comparison of Simple Potential Functions for Simulating Liquid Water. *J Chem Phys.* 1983; 79:926–935.
58. Vanommeslaeghe K, et al. CHARMM general force field: A force field for drug-like molecules compatible with the CHARMM all-atom additive biological force fields. *J Comput Chem.* 2010; 31:671–690. [PubMed: 19575467]
59. Lomize MA, Pogozheva ID, Joo H, Mosberg HI, Lomize AL. OPM database and PPM web server: resources for positioning of proteins in membranes. *Nucleic Acids Res.* 2012; 40:D370–D376. [PubMed: 21890895]
60. Jo S, Lim JB, Klauda JB, Im W. CHARMM-GUI Membrane Builder for Mixed Bilayers and Its Application to Yeast Membranes. *Biophys J.* 2009; 97:50–58. [PubMed: 19580743]
61. Berendsen HJC, Postma JPM, Vangunsteren WF, Dinola A, Haak JR. Molecular-Dynamics with Coupling to an External Bath. *J Chem Phys.* 1984; 81:3684–3690.
62. Bussi G, Donadio D, Parrinello M. Canonical sampling through velocity rescaling. *J Chem Phys.* 2007; 126:014101. [PubMed: 17212484]
63. Parrinello M, Rahman A. Polymorphic Transitions in Single-Crystals - a New Molecular-Dynamics Method. *J Appl Phys.* 1981; 52:7182–7190.

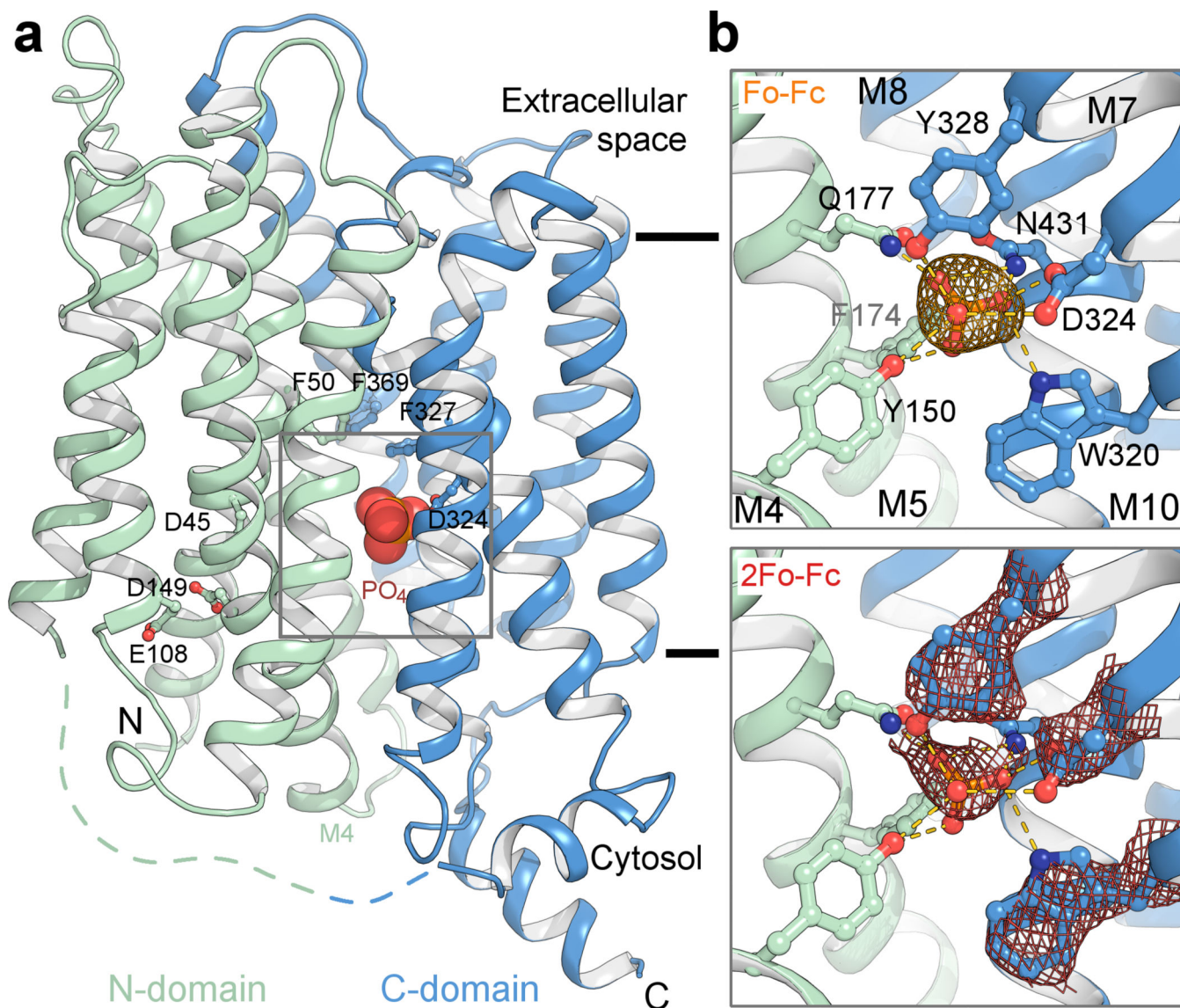


Figure 1. Structure of the High Affinity Phosphate Transporter, PiPT

The structure represents an inward facing occluded state of the phosphate transporter in complex with phosphate. **a**, Phosphate (shown as spheres) is buried in the membrane at the interface between the N-domain (pale green) and C-domain (blue). Selected residues are shown as sticks. Black bars depicts the approximate location of the membrane. **b**, The phosphate binding site with yellow dashes indicate possible hydrogen bonds (2.2–3.8 Å distances) to phosphate. *Top*, The omit $mF_{\text{obs}}-DF_{\text{calc}}$ density for phosphate is contoured in orange (4σ). *Bottom*, The $2mF_{\text{obs}}-DF_{\text{calc}}$ density for phosphate and selected M7 residues is contoured in red (2σ). Other residues are omitted for clarity (Supplementary Fig. 4e).

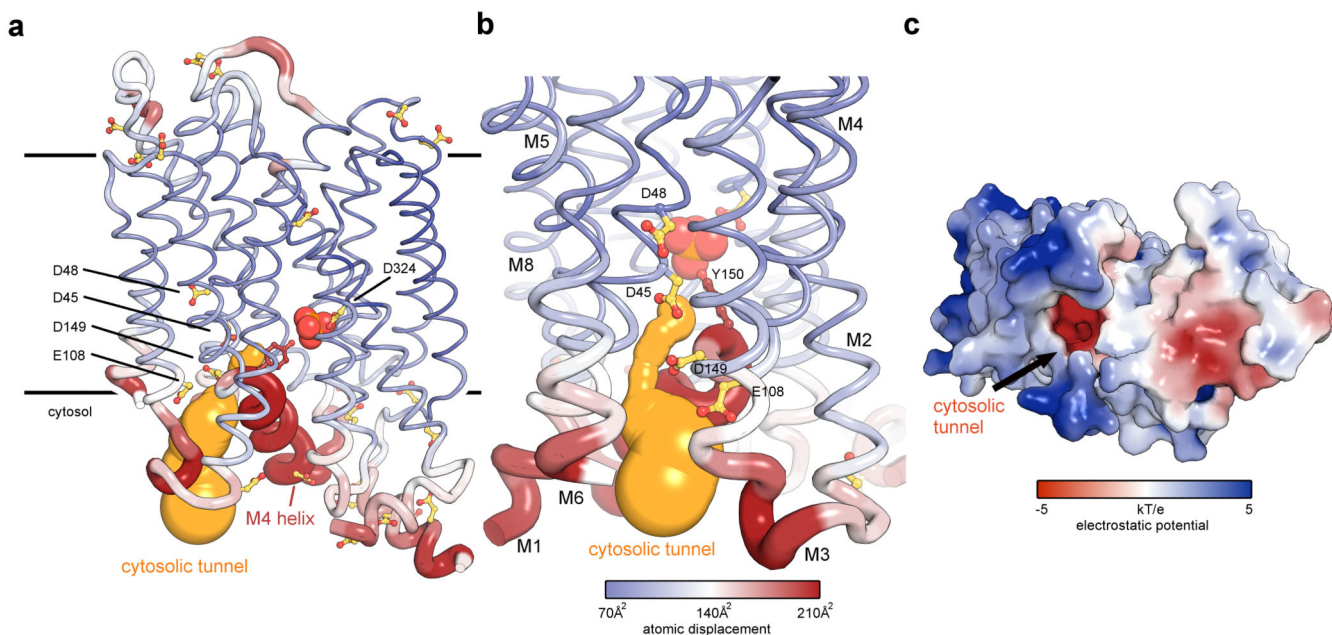


Figure 2. The proposed proton exit pathway

a, All carboxylates are shown as yellow sticks. Four carboxylate side chains in addition to Asp 324 lie in the transmembrane region and all surround the observed tunnel. The tunnel, putatively a proton conductance pathway, is too narrow for phosphate (smallest diameter 1.2 Å). The M4 helix which forms part of the tunnel has high flexibility, indicated by the atomic displacement coded by thickness of the main-chain and a colour-gradient from blue (low disorder) to red (high disorder). The average atomic displacement parameter is 107 Å² for the protein chain and 185 Å² for the cytosolic half of the M4 helix (Supplementary Fig. 4f). **b**, Rotated 90° about the vertical axis the carboxyls line the cytosolic tunnel. **c**, Electrostatic (−5 to 5 kT/e) surface representation of PiPT (cytosolic side) highlights the negative potential found in the tunnel. The phosphate oxygens are visible via the tunnel.

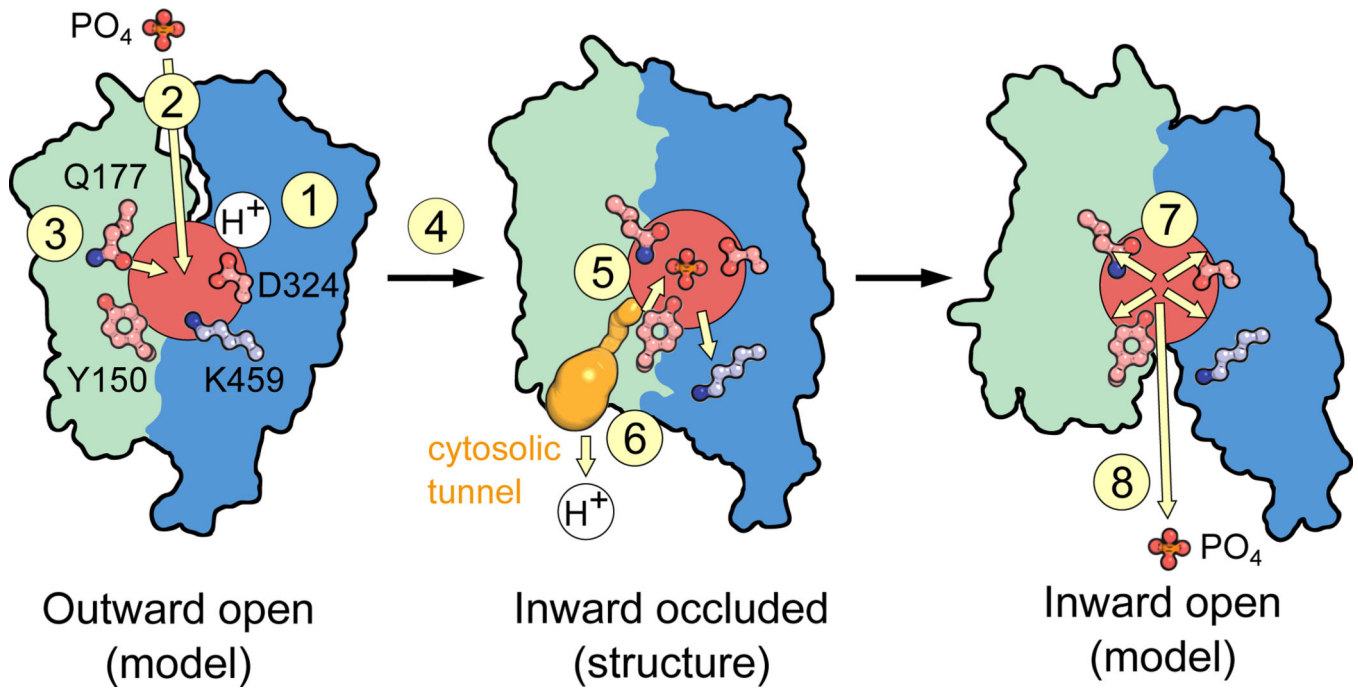


Figure 3. Proposed mechanism of phosphate transport

Asp324 is the central proton donor/acceptor of the transporter, found at the centrally located binding site (red) in the inward occluded state described (center). Models of outward open (left) and inward open (right) forms of PiPT were made by structural alignment with the fucose/proton symporter (pdb 3O7Q) and the Lactose permease (pdb 2CFQ) respectively. In the outward open conformation, the protonated form of Asp324 (1) gives preference to phosphate binding (2). Optimal binding of phosphate requires Gln177 and possible other residues to pull the N-domain towards the binding site (3), forming an outward occluded state. Conformational movements (4) opens up the tunnel in the inward occluded state (5). Exposure of the negatively charged cytosolic tunnel pulls a proton from the binding site (6) and the resulting repulsion between phosphate and the now deprotonated binding site (7) allows phosphate to exit to the cytosol between the two domains (8).